Scott Chelsea, Phipps (Orcid ID: 0000-0002-3884-4693)
Klinger Yann (Orcid ID: 0000-0003-2119-6391)
Nissen Edwin (Orcid ID: 0000-0002-0406-2706)
Maruyama Tadashi (Orcid ID: 0000-0002-1749-5885)
Arrowsmith Ramon (Orcid ID: 0000-0003-1756-3697)

2016 M7 Kumamoto, Japan, Earthquake Slip Field Derived From a Joint Inversion of Differential Lidar Topography, Optical Correlation, and InSAR Surface Displacements

Chelsea Scott, Arizona State University, USA
Johann Champenois, Institut de Physique du Globe, France
Yann Klinger, Institut de Physique du Globe- CNRS, France
Edwin Nissen, University of Victoria, Canada
Tadashi Maruyama, Geological Survey of Japan, AIST, Japan
Tatsuro Chiba, Asia Air Survey Co., Japan
Ramon Arrowsmith, Arizona State University, USA

Corresponding author:
Chelsea Scott
School of Earth and Space Exploration
ISTB4, Room 795
781 Terrace Rd, Tempe, AZ 85287-6005
Email: cpscott1@asu.edu

- We conduct an earthquake slip inversion using differential lidar topography, optical image correlation, and InSAR imagery
- We show how each dataset constrains the variable fault slip
- The apparent shallow slip deficit may reflect shallow off-fault deformation

Key words: earthquake deformation, earthquake source inversion, shallow slip, lidar, InSAR, optical correlation, geodesy

This article has been accepted for publication and undergone full peer review but has not been through the copyediting, typesetting, pagination and proofreading process which may lead to differences between this version and the Version of Record. Please cite this article as doi: 10.1029/2019GL082202

Abstract
Observations of surface deformation within 1-2km of a surface rupture contain invaluable information about the coseismic behavior of the shallow crust. We investigate the oblique strike-slip 2016 M7 Kumamoto, Japan, earthquake which ruptured the Futagawa-Hinagu Fault. We solve for variable fault slip in an inversion of differential lidar topography, satellite optical image correlation, and InSAR-derived surface displacements. The near-fault differential lidar pose several challenges. The model fault geometry must follow the surface trace at the sub-kilometer scale. Integration of displacement datasets with different sensitivities to the 3D deformation field and varying spatial distribution permits additional complexity in the inferred slip but also introduces ambiguity that requires careful selection of the regularization. We infer a $M_w 7.09^{+0.03}_{-0.05}$ earthquake. The maximum slip of 6.9m occurred at 4.5km depth, suggesting an on-fault slip deficit in the upper several kilometers of the crust that likely reflects distributed and inelastic deformation within the shallow fault zone.

Plain Language Summary
Coseismic slip inversions quantify fault slip over a fault surface and serve as critical input into research on rupture propagation, earthquake triggering, and seismic hazard. However, coseismic slip distributions are rarely constrained by observations of surface displacement immediately adjacent to the fault rupture. This limits the quality of slip models within the shallowest crust. We solve for the slip field of the 2016 M7 Kumamoto, Japan, earthquake throughout the seismogenic crust using near- and far-field observations from differential lidar topography, satellite optical image correlation, and InSAR surface displacements. The near-field differential lidar topography is critical for measuring shallow fault slip. We infer a $M_w 7.09^{+0.03}_{-0.05}$ earthquake and a maximum slip of 6.9 m at 4.5 km depth. This represents a shallow fault slip deficit where slip is greater at depth than at the surface. The missing shallow along-fault slip is accommodated as off-fault and inelastic deformation, presumably along secondary faults and folds in the shallow crust. Future earthquakes are also likely to be measured with different surface displacement datatypes. Researchers will have new opportunity to learn about the behavior of the shallow fault zone but will also be presented with technical challenges such as those discussed here.

1. Introduction

Recent advances in geodetic imaging have filled a previous near-fault data gap to reveal co- and post-seismic surface deformation along faults and in the surrounding fault volume (Brooks et al., 2017; DeLong et al., 2016; Milliner et al., 2015; Nissen et al., 2012, 2014; Oskin et al., 2012; Scott et al., 2018; Vallage et al., 2015). Inferences of both depleted and elevated shallow slip and off-fault deformation along strike and at depth in different earthquakes have raised questions about the strain budget throughout the seismic cycle. The term 'shallow-slip deficit' (e.g., Fialko et al., 2005; Simons et al., 2002) refers to a depletion of slip in the upper several kilometers of the crust, although recent work suggests that the slip deficit be an artefact of the data resolution or may not describe the behavior of all earthquakes (e.g., Xu et al., 2016). Ultimately, quantifying the variability of coseismic slip over the fault surface is critical for accurately mapping crustal strain release throughout the seismic cycle and characterizing controls on shallow fault behavior (Gold et al., 2015; Milliner et al., 2016; Teran et al., 2015; Zinke et al., 2014). Additionally, this information helps refine inferences of slip rate from paleoseismic, geomorphic, and geologic records (Dolan & Haravitch, 2014).

The M7 2016 Kumamoto ruptured the Futagawa- Hinagu Fault Zone (FHFZ) on Kyushu Island of southwestern Japan and produced over 2 m of surface slip. Here, we present a joint coseismic slip inversion of the Kumamoto earthquake constrained with near-field differential light detection and ranging (lidar) topography, optical image correlation, and Interferometric Synthetic Aperture Radar (InSAR) surface displacements. The near-field differential lidar topography and optical observations constrain the along- and near-fault surface displacements where InSAR imagery commonly lose coherence. We calculate fault slip throughout the seismogenic zone and discuss several challenges posed by the near-fault observations: (1) The model fault geometry must follow the curving surface rupture imaged by differential lidar topography. (2) The three datatypes measure different components of the 3D deformation field at varying spatial distributions, adding complexity to the earthquake source inversion. We quantify the influence of each dataset on the variable fault slip. (3) We discuss approaches for weighting and regularizing the slip inversion. We show an apparent on-fault slip deficit within the upper 2-3 km of the crust. Likely, this observation reflects off-fault and largely inelastic deformation accommodated as distributed strain within the fault volume.

2. Tectonic setting and the Kumamoto earthquake

The 2016 Kumamoto earthquake sequence ruptured the FHFZ of Kyushu island (Figure 1), which is situated on the Eurasian plate and overlies the Nankai trough where the Philippine Sea plate subducts. The right-lateral M_{ja} 6.5 (M_w 6.2) and M_{ja} 6.4 (M_w 6.0) foreshocks of 14 April and 15 April, respectively, ruptured the northern part of the Hinagu fault (T. Kobayashi, 2017). The 16 April M_{ja} 7.3 (M_w 7.0) mainshock propagated ENE for ~40 km along the Hinagu and the adjacent NNW-dipping Futagawa fault, with right-lateral and normal (uplift to the southeast) motion (Kubo et al., 2016; Moya et al., 2017; Shirahama et al., 2016). The earthquake ruptured the left-lateral conjugate shear zone and bifurcated into northern and southern ruptures that accommodate dominantly right-lateral and vertical motion (Figure 1B: Bi), respectively (Shirahama et al., 2016). Aso Caldera is likely responsible for terminating the rupture (Yagi et al., 2016). The earthquake caused intense ground shaking and damage throughout central Kyushu and killed over 100 people.

Multiple research groups produced coseismic slip models using strong motion (Asano & Iwata, 2016; Uchide et al., 2016), teleseismic (Yagi et al., 2016), long-period surface waves, GNSS, InSAR (Fukahata & Hashimoto, 2016), radar pixel tracking datasets (Himematsu & Furuya, 2016), or a combination of multiple datasets (Hao et al., 2017; Jiang et al., 2017; T. Kobayashi, 2017; Zhang et al., 2018). The fault geometry varies between the slip models. The Hinagu and Futagawa faults dip 60-80° N and 60-87° NNW, respectively, although in most models the Hinagu fault is the steeper of the two. Inferred magnitudes generally vary from M_w 7.0-7.1, and the maximum fault slip varies from 5 m to more than 6 m.

3. Data and Methods

3.1 Data:

3.1.1 Differential topography: The first lidar dataset (Chiba, 2018a) was acquired on 15 April 2016 following the foreshock activity and the second dataset was acquired on 23 April 2016 (Chiba, 2018b). The lidar point clouds have shot densities of 2.5 and 3.5 points/m^2, respectively. Scott et al. (2018) calculate 50 m resolution surface displacements from pre- and post-earthquake lidar topography using a windowed implementation of the Iterative Closest Point (ICP; Besl & McKay, 1992; Chen & Medioni, 1992) algorithm as shown in Figure 2C. We use these displacements as input to the slip inversion.

3.1.2 Optical correlation: We measure horizontal displacements by correlating 10 m resolution optical imagery collected by the Sentinel-2 satellite on 3 March 2016 and 16 February 2017 (Figure 2E) and processed using the open-source software package MicMac (Rosu et al., 2015; Rupnik et al., 2016). Cloud cover prevents us from using imagery that more closely brackets the earthquake.

There are two primary sources of noise in the optical data. First, image-parallel stripes are introduced by the sensor from a push-broom effect (e.g., Barnhart et al., 2014; Stumpf et al., 2018). We mitigate the impact of this source of noise by estimating its spatial characteristics in an area unaffected by the earthquake (Klinger et al., 2018). We apply the estimated correction to the full image. A second noise source reflects the different processing levels of imagery acquired at different times by the European Space Agency.

3.1.3 InSAR: Jiang et al. (2017) measure line-of-sight surface displacements using C-band (5.6 cm wavelength) Sentinel-1 A/B satellite Terrain Observation by Progressive Scans (TOPS) data. They exploit the large range bandwidth of TOPS data and use split-band interferometry to produce displacements that remain relatively coherent near the fault. We use the published displacements produced using range split-band interferometry and standard interferometry from ascending track 156 (Figure 2F) and descending track 163 (Figure 2G), respectively.

3.1.4 Downsampling: An earthquake slip inversion with the full set of 10^5-10^6 lidar and optical surface displacement data points is computationally infeasible. We use the triangular-based fault resolution algorithm developed by Lohman & Simons (2005) and McGuire et al. (2015) to downsample the lidar and optical datasets. This algorithm performs less spatial averaging near the fault to retain the high near-field information from both datasets. Table S2 shows the number data points after downsampling, and Figures S1-2 show the slip inversion results with the downsampled data. The InSAR imagery from Jiang et al. (2017) is already downsampled to a suitable resolution.

3.1.5 Pre- and post-seismic displacements: The datasets span different portions of the pre- and post-seismic time periods and likely record different amounts of deformation before and after the earthquake. Although we do not make any correction for the non-coseismic deformation, we consider the magnitude of deformation produced by the foreshock and post-seismic activity when comparing the slip inversion fit to the different datasets. The differential lidar topography is the only dataset that does not span either $\geq M_w$ 6 foreshocks. The M_w 6.2 14 April foreshock (Figure 1B) produced ~1.2 m of slip at its 12 km deep epicenter and ~1 m at the surface (Asano & Iwata, 2016). The post-event lidar and InSAR imagery were acquired within one week of the mainshock, yet the post-event optical imagery was acquired in February 2017. GPS data show displacements of ~10 cm directly above the ruptured fault and far-field displacements of ~5-15 cm in the first 91 days following the mainshock (Moore et al., 2017).

3.2 Fault geometry

Typically, the fault geometry of >M7 earthquakes used in earthquake source inversions consists of multiple rectangular fault segments that each have a constant strike and dip (e.g., Barnhart et al., 2014; Huang et al., 2017; Marchandon et al., 2018; Wei et al., 2011). The use of a curving fault is rare (Wang et al., 2013). The slip inversion for the Kumamoto earthquake requires a kinking surface trace due to the complex fault geometry revealed by the differential lidar topography (Figure 1). We damp the kinking at depth, so that the fault

becomes increasingly planar at depth where local complexities in the fault geometry are poorly constrained (Figure 2B). Because data resolution of slip decreases with depth (Motagh et al., 2006; Simons et al., 2002), we increase the area of the subfaults from less than 1 km^2 near the surface to 15 km^2 at 20 km depth using Barnhart & Lohman (2010)'s approach. The Futagawa and Hinagu faults dip 65° and 72°, respectively, consistent with foreshock and aftershock locations (Lin et al., 2016), published slip models (e.g., Asano & Iwata, 2016), and surface fault exposures (Shirahama et al., 2016). Faults extend to a maximum depth of 20 km. Where the Futagawa Fault steps to the left at the eastern extent of the lidar coverage, the fault geometry is discontinuous at the surface yet remains connected from 1 km depth to the down dip extent of the fault.

3.3 Slip inversion and regularization

We conduct two sets of joint inversions for variable slip using surface displacements derived from combined (1) lidar-optical-InSAR and (2) optical-InSAR imagery. Here, we outline our approach for the joint lidar-optical-InSAR slip inversion. The approach for the optical-InSAR slip inversion (Figures S3-4) is identical, except we omit the lidar data. We consider the forward fault slip problem,

$$\mathbf{G}\mathrm{m} = \mathrm{d} \quad \textbf{(1)}$$

Where $\boldsymbol{G}$ is the set of Green's functions that relate fault slip along triangular dislocations (m) embedded in an elastic isotropic halfspace (Meade, 2007) to surface displacements (d). The InSAR phase delays and optical displacements are observed relative to an arbitrary zero level due to satellite orbital errors, resulting in long wavelength errors in the measured displacement fields (e.g., Fattahi & Amelung, 2014; Hanssen, 2001). To account for these errors, we add terms to **G** that remove a bilinear ramp (e.g., Bekaert et al., 2016) from each of the optical and the two InSAR datasets. We do not add equivalent terms for the lidar dataset, because the two lidar surveys are tied to the same external reference frame through GPS. We assume a Poisson's ratio of 0.25 and a shear modulus of $3.0\text{x}10^{11}$ dyne/cm^2.

We apply several constraints to the slip inversion. (1) We select a relative weighting between each of the three datatypes so that each datatype has a similar constraint on the inferred slip distribution (Table S2). (2) The rake varies, but we add positivity constraints to force right-lateral and normal dip-slip motion. (3) We apply Tikhonov Laplacian regularization along each fault.

The preferred slip distribution minimizes the norm (Aster et al., 2013; Menke, 1984):

$$\min \left| \begin{bmatrix} \boldsymbol{G}_w \\ \lambda \boldsymbol{L} \end{bmatrix} m - \begin{bmatrix} d_w \\ 0 \end{bmatrix} \right|, \quad \textbf{(2)}$$

Where $\boldsymbol{L}$ is regularization matrix, and is the regularization parameter. The optimal lies at the L-curve corner produced by solving the slip inversion with different regularization parameters (Harris & Segall, 1987). Our quoted uncertainty of the earthquake magnitude reflects the range of magnitudes associated with slip models that lie within the broad L-curve corner, shown by the black uncertainty curve.

The generalized inverse is,

$$\boldsymbol{G^{-g}} = \left(\begin{bmatrix} G_w \\ \lambda L \end{bmatrix}^T \begin{bmatrix} G_w \\ \lambda L \end{bmatrix} \right)^{-1} G_w^T. \quad \textbf{(3)}$$

The slip inversion is solved by:

$$\boldsymbol{m} = \boldsymbol{G}^{-\boldsymbol{g}}\, d. \quad \textbf{(4)}$$

3.4 Dataset resolution for variable fault slip

When datasets with varying sensitivity to the 3D surface deformation field and spatial distributions are combined in a joint slip inversion, knowledge about how each dataset constrains the variable slip field serves as a critical constraint on the slip inversion quality. We extend Barnhart & Lohman (2010)'s technique and calculate how each dataset resolves the slip field. The resolving power *R* at subfault *i* from dataset *j* is the norm of the terms in G^{-g} whose row corresponds to fault patch *i* and columns to dataset *j*:

$$R_{\boldsymbol{patch\ i,dataset\ j}} = |\boldsymbol{G}^{-\boldsymbol{g}}(\boldsymbol{patch}_i, \boldsymbol{d}_j)|. \quad \textbf{(5)}$$

Due to the non-linear positivity constraints, the slip inversion is non-linear. Therefore *R* is only an approximate measure of the data resolution. Figure 3AB shows the dataset with the greatest *R* for each subfault. We calculate the resolving power at specific depths ($R_{\text{depth i, dataset j}}$) by taking the norm of R for the set of subfaults located 1.5 km above or below $depth_i$ (Figure 3C):

$$R_{\boldsymbol{depth\ i,dataset\ j}} = \sqrt{\sum_{k=1}^{N} R_{\boldsymbol{patch\ k,dataset\ j}}^{\,2}}. \quad \textbf{(6)}$$

At each depth range, we normalize the combined resolving power of all datasets to unity.

4. Results and discussion

4.1 Joint earthquake source inversion

The lidar-optical-InSAR slip inversion (Figure 2A) calculates a $M_w\ 7.09^{+0.03}_{-0.05}$ earthquake given the assumed elastic half-space parameters (Figure 4A) and uncertainty reflecting the regularization choice. The earthquake ruptured a 40 km along-strike length and a 20 km width. It produced a maximum slip of 6.9 m at 4.5 km depth along the eastern section of the Hinagu Fault. Slip is lower in magnitude and less concentrated along the Futagawa Fault relative to the Hinagu Fault. Slip decreases rapidly past Aso Caldera.

The lidar-optical-InSAR inversion reproduces the first-order displacement fields of the three datatypes. The largest differential lidar topography residuals (Figure 2CD) occur near the fault and reflect a combination of an oversimplified fault geometry, off-fault deformation, and the elastic rheology assumption. The E-W optical data appear to show a narrower deformation signal than is produced by the slip inversion (Figure 2E). In contrast, the ascending InSAR imagery (Figure 2F) record a broader signal than is captured by the slip model. Postseismic deformation cannot explain the differences in model fit between the two data types, because the InSAR data were acquired 10 months prior to the optical data. Because the residual optical deformation signal (Figure 2E) contains N-NNE oriented stripes immediately adjacent to the fault, we propose that the optical data misfit reflects the satellite's push boom error.

For the optical-InSAR slip inversion, we infer a $M_w\ 7.10^{+0.02}_{-0.02}$. The earthquake produces at maximum slip of 5.2 m at 1.3 km depth. There is a similar quality of fit to the surface displacements for both the lidar-optical-InSAR and the optical-InSAR earthquake source inversions.

The lidar-optical-InSAR inversion places the maximum slip and 61% of the total moment release on the Hinagu Fault while the optical-InSAR places the maximum slip on the Futagawa fault and equal moment release on both faults. As shown in Figure 4C, the fault that hosts the maximum moment release depends on the regularization. For the lidar-optical-

InSAR inversion, the Hinagu fault hosts the greatest moment release at the L-curve corner. For both inversions, the moment release shifts towards the Futagawa Fault with increasing regularization. For all regularization values, the lidar-optical-InSAR inversion resolves a greater maximum slip than the lidar-optical inversion, yet both inversions result in similar earthquake moments for the preferred slip model.

We compare our two slip fields with slip fields constrained from a strong motion seismic dataset (Asano & Iwata, 2016) and from strong motion seismic, teleseismic, and geodetic (H. Kobayashi et al., 2017) datasets in Figure 4G-J. The lidar-optical-InSAR and optical-InSAR slip models produce slip that is shallow (i.e., closer to the fault trace) and localized to either the Hinagu Fault or the central portion of the Futagawa Fault relative to the slip models from Asano & Iwata (2016) and H. Kobayashi et al. (2017). The difference in slip concentration likely reflects the broader spatial distribution of the seismic data used to constrain the latter two slip fields.

4.2 Data constraints on fault slip as a function of depth

The differential lidar topography constrain shallow strike-slip and dip-slip motion within the lidar footprint denoted by the black arrows in Figure 3AB. The optical imagery constrain the majority of the remaining strike-slip motion and some dip-slip motion above 5 km depth. The InSAR imagery from both flight directions constrain deeper slip. Within the lidar footprint, differential topography dominantly constrains fault slip above 7 km (Figure 3C; dashed lines). Because the optical imagery constrain near- and far-field slip, the imagery have a fairly constant resolving power with depth and resolve less shallow slip than the differential topography.

4.3 Regularization

As commonly observed, the regularization choice impacts the inferred slip distribution. Increasing the amount of regularization (i.e., higher λ) decreases the maximum slip for both sets of earthquake source inversions (Figure 4B). For the range of regularization values, the lidar-optical-InSAR inversion resolves a greater maximum slip than the optical-InSAR inversion. This may reflect that the greater density of differential lidar topography near the fault require more concentrated slip and a higher slip magnitude. The moment release migrates from the Hinagu to the Futagawa Fault with increasing regularization (Figure 4C). The lidar-optical-InSAR inversion places additional moment release on the Hinagu fault, possibly because the differential lidar topography require two overlapping faults near the intersection of the Futagawa and Hinagu Faults. In contrast, the optical and InSAR (Jiang et al., 2017) datasets can be well-modeled with a single curving fault. Huang et al. (2017) observed that the regularization affects the depth-profile of slip for the 2010 M7.2 El Mayor Cucapah earthquake. It remains important to test the impact of the regularization in joint slip inversions, particularly as more datatypes are ingested into slip inversions.

4.4 Shallow fault slip behavior

We examine the median slip versus depth for the Hinagu (Figure 4D) and the Futagawa Faults (Figure 4E) and the entire earthquake (Figure 4F) for the lidar-optical-InSAR (blue) and optical-InSAR (red) slip inversions. The shallow slip deficit along the Hinagu Fault from the lidar-optical-InSAR slip inversion may indicate that the earthquake did not yet have sufficient energy to rupture through the velocity-strengthening portion of the shallow crust.

Both the lidar-optical-InSAR and optical-InSAR inversions show similar behavior for the Futagawa Fault; a median slip of ~2 m at depths of 1-4 km and a decrease in slip within the

upper 1 km of the crust. We interpret this observation to reflect a slip deficit along the primary fault trace yet not a shallow strain deficit in the 3D fault volume. Approximately half of the total shallow deformation was accommodated off the principal fault and the region of inelastic deformation straddled the fault by 250 m (Scott et al., 2018). The 1905 Tsetserleg-Bulnay (Choi et al., 2018), 1999 Izmit (Rockwell et al., 2002), and 2013 Balochistan (Vallage et al., 2015) earthquakes produced similar off-fault deformation. Likely, the off-fault deformation was accommodated as volume change (Scott et al. 2018) and as slip along secondary faults in a flower-like structure that was not explicitly included in the fault geometry. In the slip inversion, the shallow and off-fault deformation was mapped as deeper on-fault slip, resulting in an apparent shallow slip deficit. Further, inelastic deformation produces a lower strain than elastic deformation (Kaneko & Fialko, 2011), suggesting that a portion of the apparent shallow slip deficit reflects the assumed rheology. Future work should focus on using an inverse modeling approach to solve for strain within the 3D fault volume (Mossop & Segall, 1999; Okada, 1985) in addition to slip along individual faults.

5. Conclusions

We develop the first lidar-optical-InSAR earthquake source inversion that resolves slip throughout the seismogenic crust. We quantify depth-dependent variations in fault slip, which are important for understanding the strain budget of the shallow crust. The surface deformation produced by future earthquakes is likely to be recorded by hybrid datasets with varying spatial distribution and sensitivity to the 3D deformation field. Such joint inversions will provide new opportunity to learn about the behavior of the shallow fault zone but will also present challenges such as those discussed here. We discuss new approaches and model refinements for performing coseismic slip inversions using near-field observations. We learn the following: (1) The model fault geometry must follow the surface trace at a scale appropriate for the finest resolution data. (2) The amount of regularization impacts the inferred fault slip. (3) Off-fault deformation may be incorrectly interpreted as deeper and on-fault slip. Future work should consider approaches for directly accounting for off-fault deformation in the 3D fault volume.

6. Acknowledgements

C. Scott was supported by NSF Postdoctoral Fellowship 1625221 and by the School of Earth and Space Exploration at Arizona State University. JC and YK were funded by IRSN and the Tosca-CNES Program. EN was supported by the Canada Research Chair program and by the Natural Sciences and Engineering Research Council of Canada through Discovery Grant 2017-04029. We thank editor Lucy Flesch and two anonymous reviewers for constructive comments.

The lidar and InSAR data is published and available from Chiba (2018a), Chiba (2018b), and Jiang et al. (2017). The Sentinel-2 data is freely available from the European Space Agency (https://scihub.copernicus.eu/dhus/#/home) and can be processed using the open-source software package MicMac.

7. References

Asano, K., & Iwata, T. (2016). Source rupture processes of the foreshock and mainshock in the 2016 Kumamoto earthquake sequence estimated from the kinematic waveform inversion of strong motion data. *Earth, Planets and Space*, *68*(1). https://doi.org/10.1186/s40623-016-0519-9.

Aster, R., Borchers, B., & Thurber, C. (2013). *Parameter Esimation and Inverse Problems* (2nd ed.). Amsterdam: Academic Press.

Barnhart, W. D., & Lohman, R. B. (2010). Automated fault model discretization for inversions for coseismic slip distributions. *Journal of Geophysical Research*, *115*(B10). https://doi.org/10.1029/2010JB007545.

Barnhart, W. D., Hayes, G. P., Briggs, R. W., Gold, R. D., & Bilham, R. (2014). Ball-and-socket tectonic rotation during the 2013 M w 7.7 Balochistan earthquake. *Earth and Planetary Science Letters*, *403*, 210–216. https://doi.org/10.1016/j.epsl.2014.07.001.

Bekaert, D. P. S., Segall, P., Wright, T. J., & Hooper, A. J. (2016). A Network Inversion Filter combining GNSS and InSAR for tectonic slip modeling. *Journal of Geophysical Research: Solid Earth*, *121*(3), 2069–2086. https://doi.org/10.1002/2015JB012638.

Besl, P. J., & McKay, N. D. (1992). A method for registration of 3-D shapes. *IEEE Transactions on Pattern Analysis and Machine Intelligence*, *14*(2), 239–256. https://doi.org/10.1109/34.121791.

Brooks, B. A., Minson, S. E., Glennie, C. L., Nevitt, J. M., Dawson, T., Rubin, R., et al. (2017). Buried shallow fault slip from the South Napa earthquake revealed by near-field geodesy. *Science Advances*, *3*(7), e1700525. https://doi.org/10.1126/sciadv.1700525.

Chen, Y., & Medioni, G. (1992). Object modelling by registration of multiple range images. *Image and Vision Computing*, *10*(3), 145–155. https://doi.org/10.1016/0262-8856(92)90066-C.

Chiba, T. (2018a). Pre-Kumamoto Earthquake (16 April 2016) Rupture Lidar Scan airborne lidar survey. Air Asia Survey Co., Ltd, distributed by OpenTopography. Retrieved from https://doi.org/10.5069/G9XP7303.

Chiba, T. (2018b). Post-Kumamoto Earthquake (16 April 2016) Rupture Lidar Scan airborne lidar survey. Air Asia Survey Co., Ltd, distributed by OpenTopography. Retrieved from https://doi.org/10.5069/G9SX6B9T.

Choi, J.-H., Klinger, Y., Ferry, M., Ritz, J.-F., Kurtz, R., Rizza, M., et al. (2018). Geologic Inheritance and Earthquake Rupture Processes: The 1905 M ≥ 8 Tsetserleg-Bulnay Strike-Slip Earthquake Sequence, Mongolia. *Journal of Geophysical Research: Solid Earth*, *123*(2), 1925–1953. https://doi.org/10.1002/2017JB013962.

DeLong, S. B., Donnellan, A., Ponti, D. J., Rubin, R. S., Lienkaemper, J. J., Prentice, C. S., et al. (2016). Tearing the terroir: Details and implications of surface rupture and deformation from the 24 August 2014 *M* 6.0 South Napa earthquake, California: Napa Earthquake. *Earth*

and Space Science, *3*(10), 416–430. https://doi.org/10.1002/2016EA000176.

Dolan, J. F., & Haravitch, B. D. (2014). How well do surface slip measurements track slip at depth in large strike-slip earthquakes? The importance of fault structural maturity in controlling on-fault slip versus off-fault surface deformation. *Earth and Planetary Science Letters*, *388*, 38–47. https://doi.org/10.1016/j.epsl.2013.11.043.

Fattahi, H., & Amelung, F. (2014). InSAR uncertainty due to orbital errors. *Geophysical Journal International*, *199*(1), 549–560. https://doi.org/10.1093/gji/ggu276.

Fialko, Y., Sandwell, D., Simons, M., & Rosen, P. (2005). Three-dimensional deformation caused by the Bam, Iran, earthquake and the origin of shallow slip deficit. *Nature*, *435*(7040), 295–299. https://doi.org/10.1038/nature03425.

Fukahata, Y., & Hashimoto, M. (2016). Simultaneous estimation of the dip angles and slip distribution on the faults of the 2016 Kumamoto earthquake through a weak nonlinear inversion of InSAR data. *Earth, Planets and Space*, *68*(1). https://doi.org/10.1186/s40623-016-0580-4.

Gold, R. D., Reitman, N. G., Briggs, R. W., Barnhart, W. D., Hayes, G. P., & Wilson, E. (2015). On- and off-fault deformation associated with the September 2013 Mw 7.7 Balochistan earthquake: Implications for geologic slip rate measurements. *Tectonophysics*, *660*, 65–78. https://doi.org/10.1016/j.tecto.2015.08.019.

Hanssen, R. (2001). *Radar Interferometry: Data Interpretation and Error Analysis* (Vol. 2). Dordrecht: Kluwer Academic Press.

Hao, J., Ji, C., & Yao, Z. (2017). Slip history of the 2016 M_w 7.0 Kumamoto earthquake: Intraplate rupture in complex tectonic environment: Slip History of 2016 Kumamoto Earthquake.
Geophysical Research Letters, *44*(2), 743–750. https://doi.org/10.1002/2016GL071543.

Harris, R. A., & Segall, P. (1987). Detection of a locked zone at depth on the Parkfield, California, segment of the San Andreas Fault. *Journal of Geophysical Research*, *92*(B8), 7945. https://doi.org/10.1029/JB092iB08p07945.

Himematsu, Y., & Furuya, M. (2016). Fault source model for the 2016 Kumamoto earthquake sequence based on ALOS-2/PALSAR-2 pixel-offset data: evidence for dynamic slip partitioning. *Earth, Planets and Space*, *68*(1). https://doi.org/10.1186/s40623-016-0545-7.

Huang, M.-H., Fielding, E. J., Dickinson, H., Sun, J., Gonzalez-Ortega, J. A., Freed, A. M., & Bürgmann, R. (2017). Fault geometry inversion and slip distribution of the 2010 M_w 7.2 El Mayor-Cucapah earthquake from geodetic data: El Mayor-Cucapah Coseismic Displacement. *Journal of Geophysical Research: Solid Earth*, *122*(1), 607–621. https://doi.org/10.1002/2016JB012858.

Jiang, H., Feng, G., Wang, T., & Bürgmann, R. (2017). Toward full exploitation of coherent and incoherent information in Sentinel-1 TOPS data for retrieving surface displacement: Application to the 2016 Kumamoto (Japan) earthquake. *Geophysical Research Letters*.

https://doi.org/10.1002/2016GL072253.

Kaneko, Y., & Fialko, Y. (2011). Shallow slip deficit due to large strike-slip earthquakes in dynamic rupture simulations with elasto-plastic off-fault response: Modelling shallow slip deficit. *Geophysical Journal International*, *186*(3), 1389–1403. https://doi.org/10.1111/j.1365-246X.2011.05117.x.

Klinger, Y., Okubo, K., Vallage, A., Champenois, J., Delorme, A., Rougier, E., et al. (2018). Earthquake damage patterns resolve complex rupture processes. *Geophysical Research Letters*. https://doi.org/10.1029/2018GL078842.

Kobayashi, H., Koketsu, K., & Miyake, H. (2017). Rupture processes of the 2016 Kumamoto earthquake sequence: Causes for extreme ground motions: Rupture Processes of the Kumamoto Events. *Geophysical Research Letters*, *44*(12), 6002–6010. https://doi.org/10.1002/2017GL073857.

Kobayashi, T. (2017). Earthquake rupture properties of the 2016 Kumamoto earthquake foreshocks (M j 6.5 and M j 6.4) revealed by conventional and multiple-aperture InSAR. *Earth, Planets and Space*, *69*(1). https://doi.org/10.1186/s40623-016-0594-y.

Kubo, H., Suzuki, W., Aoi, S., & Sekiguchi, H. (2016). Source rupture processes of the 2016 Kumamoto, Japan, earthquakes estimated from strong-motion waveforms. *Earth, Planets and Space*, *68*(1). https://doi.org/10.1186/s40623-016-0536-8.

Lohman, R. B., & Simons, M. (2005). Some thoughts on the use of InSAR data to constrain models of surface deformation: Noise structure and data downsampling. *Geochemistry, Geophysics, Geosystems*, *6*(1), https://doi.org/10.1029/2004GC000841.

Marchandon, M., Vergnolle, M., Sudhaus, H., & Cavalié, O. (2018). Fault Geometry and Slip Distribution at Depth of the 1997 Mw 7.2 Zirkuh Earthquake: Contribution of Near-Field Displacement Data. *Journal of Geophysical Research: Solid Earth*, *123*(2), 1904–1924. https://doi.org/10.1002/2017JB014703.

McGuire, J. J., Lohman, R. B., Catchings, R. D., Rymer, M. J., & Goldman, M. R. (2015). Relationships among seismic velocity, metamorphism, and seismic and aseismic fault slip in the Salton Sea Geothermal Field region: Salton Sea Geothermal Field. *Journal of Geophysical Research: Solid Earth*, *120*(4), 2600–2615. https://doi.org/10.1002/2014JB011579.

Meade, B. J. (2007). Algorithms for the calculation of exact displacements, strains, and stresses for triangular dislocation elements in a uniform elastic half space. *Computers & Geosciences*, *33*(8), 1064–1075. https://doi.org/10.1016/j.cageo.2006.12.003

Menke, W. (1984). *Geophysical Data Analysis: Discrete Inverse Theory* (International Geophysics Series, vol. 45, Vol. 45). New York: Academic Press.

Milliner, C., Dolan, J. F., Hollingsworth, J., Leprince, S., Ayoub, F., & Sammis, C. G. (2015). Quantifying near-field and off-fault deformation patterns of the 1992 M_w 7.3 Landers earthquake: Deformation of the Landers earthquake. *Geochemistry, Geophysics, Geosystems*, *16*(5), 1577–1598. https://doi.org/10.1002/2014GC005693.

Milliner, C., Sammis, C., Allam, A. A., Dolan, J. F., Hollingsworth, J., Leprince, S., & Ayoub, F. (2016). Resolving Fine-Scale Heterogeneity of Co-seismic Slip and the Relation to Fault Structure. *Scientific Reports*, *6*(1). https://doi.org/10.1038/srep27201.

Moore, J. D. P., Yu, H., Tang, C.-H., Wang, T., Barbot, S., Peng, D., et al. (2017). Imaging the distribution of transient viscosity after the 2016 M_w 7.1 Kumamoto earthquake. *Science*, *356*(6334), 163–167. https://doi.org/10.1126/science.aal3422.

Mossop, A., & Segall, P. (1999). Volume strain within The Geysers geothermal field. *Journal of Geophysical Research: Solid Earth*, *104*(B12), 29113–29131. https://doi.org/10.1029/1999JB900284

Motagh, M., Klotz, J., Tavakoli, F., Djamour, Y., Arabi, S., Wetzel, H.-U., & Zschau, J. (2006). Combination of Precise Leveling and InSAR Data to Constrain Source Parameters of the Mw = 6.5, 26 December 2003 Bam Earthquake. *Pure and Applied Geophysics*, *163*(1), 1–18. https://doi.org/10.1007/s00024-005-0005-y.

Moya, L., Yamazaki, F., Liu, W., & Chiba, T. (2017). Calculation of coseismic displacement from lidar data in the 2016 Kumamoto, Japan, earthquake. *Natural Hazards and Earth System Sciences*, *17*(1), 143–156. https://doi.org/10.5194/nhess-17-143-2017

National Institute of Advanced Industrial Science and Technology. (2016). Active fault database of Japan. Active Fault Database of Japan.

Nissen, E., Krishnan, A. K., Arrowsmith, J. R., & Saripalli, S. (2012). Three-dimensional surface displacements and rotations from differencing pre- and post-earthquake LiDAR point clouds. *Geophysical Research Letters*, *39*(16), https://doi.org/10.1029/2012GL052460

Nissen, E., Maruyama, T., Ramon Arrowsmith, J., Elliott, J. R., Krishnan, A. K., Oskin, M. E., & Saripalli, S. (2014). Coseismic fault zone deformation revealed with differential lidar: Examples from Japanese ~7 intraplate earthquakes. *Earth and Planetary Science Letters*, *405*, 244–256. https://doi.org/10.1016/j.epsl.2014.08.031.

Okada, Y. (1985). Surface deformation due to shear and tensile faults in a half space. *Bulletin of the Seismological Society of America*, *74*, 1135–1154.

Oskin, M. E., Arrowsmith, J. R., Corona, A. H., Elliott, A. J., Fletcher, J. M., Fielding, E. J., et al. (2012). Near-Field Deformation from the El Mayor-Cucapah Earthquake Revealed by Differential LIDAR. *Science*, *335*(6069), 702–705. https://doi.org/10.1126/science.1213778

Rockwell, T. K., Lindvall, S., Dawson, T., Langridge, R., Lettis, W., & Klinger, Y. (2002). Lateral Offsets on Surveyed Cultural Features Resulting from the 1999 Izmit and Duzce Earthquakes, Turkey. *Bulletin of the Seismological Society of America*, *92*(1), 79–94. https://doi.org/10.1785/0120000809.

Rosu, A.-M., Pierrot-Deseilligny, M., Delorme, A., Binet, R., & Klinger, Y. (2015). Measurement of ground displacement from optical satellite image correlation using the free open-source software MicMac. *ISPRS Journal of Photogrammetry and Remote Sensing*, *100*, 48–59. https://doi.org/10.1016/j.isprsjprs.2014.03.002.

Rupnik, E., Pierrot Deseilligny, M., Delorme, A., & Klinger, Y. (2016). Refined Satellite Image Orientation in the Free Open-Source Photogrammetric Tools Apero/Micmac. *ISPRS Annals of Photogrammetry, Remote Sensing and Spatial Information Sciences*, *III–1*, 83–90. https://doi.org/10.5194/isprsannals-III-1-83-2016.

Scott, C. P., Arrowsmith, J. R., Nissen, E., Lajoie, L., Maruyama, T., & Chiba, T. (2018). The *M* 7 2016 Kumamoto, Japan, Earthquake: 3-D Deformation Along the Fault and Within the Damage Zone Constrained From Differential Lidar Topography. *Journal of Geophysical Research: Solid Earth*. https://doi.org/10.1029/2018JB015581.

Shirahama, Y., Yoshimi, M., Awata, Y., Maruyama, T., Azuma, T., Miyashita, Y., et al. (2016). Characteristics of the surface ruptures associated with the 2016 Kumamoto earthquake sequence, central Kyushu, Japan. *Earth, Planets and Space*, *68*(1). https://doi.org/10.1186/s40623-016-0559-1.

Simons, M., Fialko, Y., & Rivera, L. (2002). Coseismic Deformation from the 1999 Mw 7.1 Hector Mine, California, Earthquake as Inferred from InSAR and GPS Observations. *Bulletin of the Seismological Society of America*, *92*(4), 1390–1402. https://doi.org/10.1785/0120000933.

Stumpf, A., Michéa, D., & Malet, J.-P. (2018). Improved Co-Registration of Sentinel-2 and Landsat-8 Imagery for Earth Surface Motion Measurements. *Remote Sensing*, *10*(2), 160. https://doi.org/10.3390/rs10020160.

Teran, O. J., Fletcher, J. M., Oskin, M. E., Rockwell, T. K., Hudnut, K. W., Spelz, R. M., et al. (2015). Geologic and structural controls on rupture zone fabric: A field-based study of the 2010 Mw 7.2 El Mayor-Cucapah earthquake surface rupture. *Geosphere*, *11*(3), 899–920. https://doi.org/10.1130/GES01078.1

Uchide, T., Horikawa, H., Nakai, M., Matsushita, R., Shigematsu, N., Ando, R., & Imanishi, K. (2016). The 2016 Kumamoto–Oita earthquake sequence: aftershock seismicity gap and dynamic triggering in volcanic areas. *Earth, Planets and Space*, *68*(1). https://doi.org/10.1186/s40623-016-0556-4.

Vallage, A., Klinger, Y., Grandin, R., Bhat, H. S., & Pierrot-Deseilligny, M. (2015). Inelastic surface deformation during the 2013 M_w 7.7 Balochistan, Pakistan, earthquake. *Geology*, G37290.1. https://doi.org/10.1130/G37290.1.

Wang, R., Diao, F., & Hoechner, A. (2013). SDM - A geodetic inversion code incorporating with layered crust structure and curved fault geometry.

Wei, S., Fielding, E., Leprince, S., Sladen, A., Avouac, J.-P., Helmberger, D., et al. (2011). Superficial simplicity of the 2010 El Mayor–Cucapah earthquake of Baja California in Mexico. *Nature Geoscience*, *4*(9), 615–618. https://doi.org/10.1038/ngeo1213.

Xu, X., Tong, X., Sandwell, D. T., Milliner, C. W. D., Dolan, J. F., Hollingsworth, J., et al. (2016). Refining the shallow slip deficit. *Geophysical Journal International*, *204*(3), 1843–1862. https://doi.org/10.1093/gji/ggv563.

Yagi, Y., Okuwaki, R., Enescu, B., Kasahara, A., Miyakawa, A., & Otsubo, M. (2016). Rupture process of the 2016 Kumamoto earthquake in relation to the thermal structure around Aso volcano. *Earth, Planets and Space*, *68*(1). https://doi.org/10.1186/s40623-016-0492-3.

Zhang, Y., Shan, X., Zhang, G., Gong, W., Liu, X., Yin, H., et al. (2018). Source Model of the 2016 Kumamoto, Japan, Earthquake Constrained by InSAR, GPS, and Strong- Motion Data: Fault Slip under Extensional Stress. *Bulletin of the Seismological Society of America*. https://doi.org/10.1785/0120180023.

Zinke, R., Hollingsworth, J., & Dolan, J. F. (2014). Surface slip and off-fault deformation patterns in the 2013 M_W 7.7 Balochistan, Pakistan earthquake: Implications for controls on the distribution of near-surface coseismic slip. *Geochemistry, Geophysics, Geosystems*, *15*(12), 5034–5050. https://doi.org/10.1002/2014GC005538

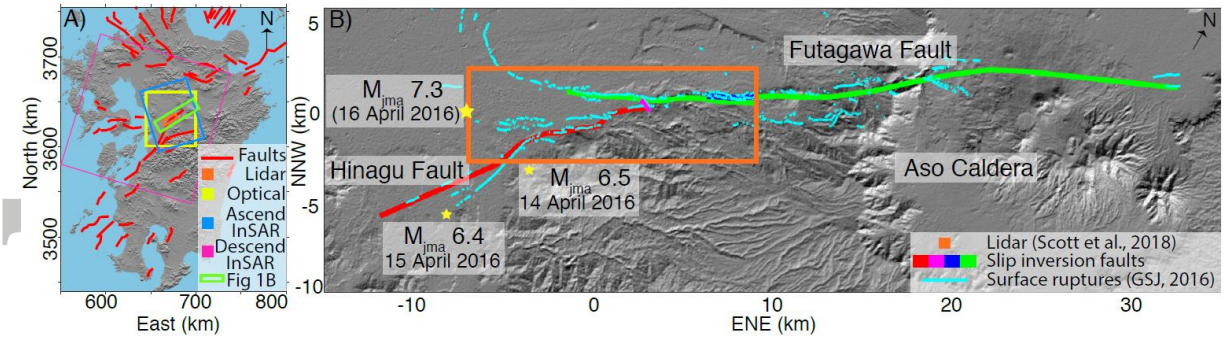

Figure 1: A) Map of the Kyushu Island, southwestern Japan, showing active faults (red; National Institute of Advanced Industrial Science and Technology, 2016) and coverage of the four datasets (UTM projection). The ascending and descending InSAR imagery represent range split-band and standard interferometry, respectively. (B) 2016 M7 Kumamoto earthquake fault map. Thin blue lines show surface ruptures mapped by AIST (2016). Red, pink, blue, and green lines show the surface traces of the faults used in the coseismic slip inversion. We refer to the entire red fault as the Hinagu Fault. See Figure 2 for the 3D fault structure. Yellow stars are foreshocks and mainshock epicenters estimated by the Japan Meteorological Agency. (B) and all subsequent figures are rotated to a ENE-NNW oriented coordinate system.

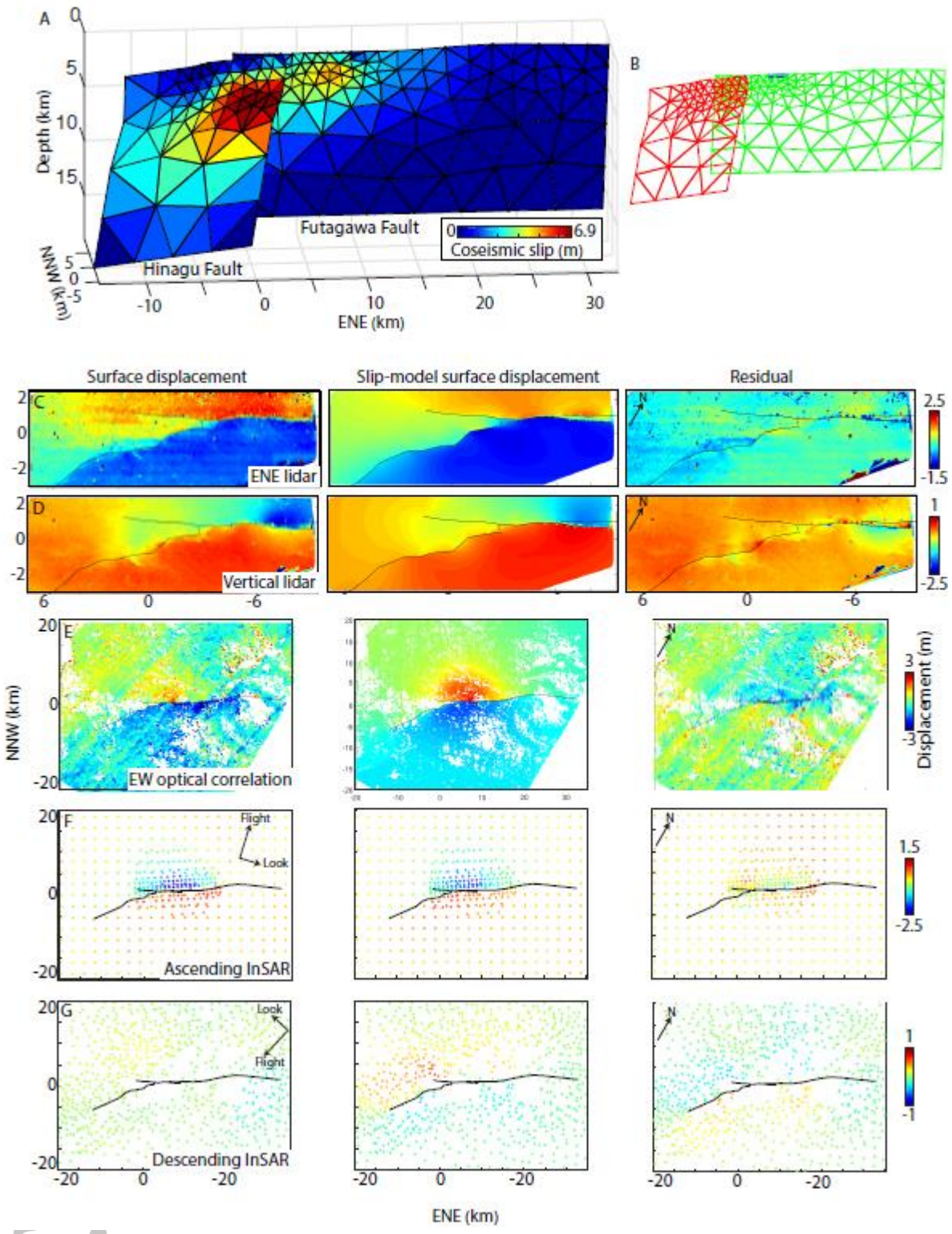

Figure 2: (A) Variable fault slip for the lidar-optical-InSAR inversion. (B) Fault geometry frame with colors corresponding to fault segments in Figure 1B. Subfaults are the individual triangles. C-G: Measured surface displacements (first column), surface displacements predicted from the preferred coseismic slip inversion (second column), and residual displacements (third column) for the ENE differential lidar topography (C), vertical differential lidar topography (D), E-W optical correlation (E), ascending InSAR (F), and descending InSAR (G).

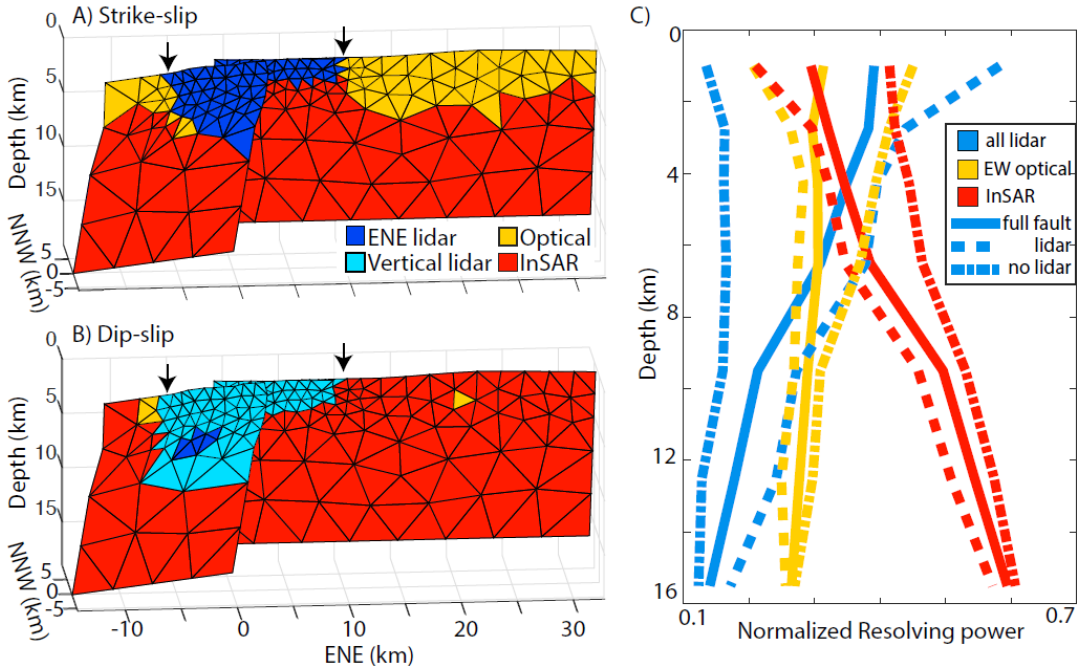

Figure 3: Data constraints on the lidar-optical-InSAR variable slip inversion. The dataset with the highest resolving power is shown for strike-slip (A) and dip-slip (B) motion. Black arrows indicate the spatial extent of the differential lidar. (C) shows depth vs. the normalized resolving power for the three datatypes along the entire fault (solid lines), the fault segment within the lidar footprint (dashed lines), and the fault segment outside of the lidar coverage (dotted lines).

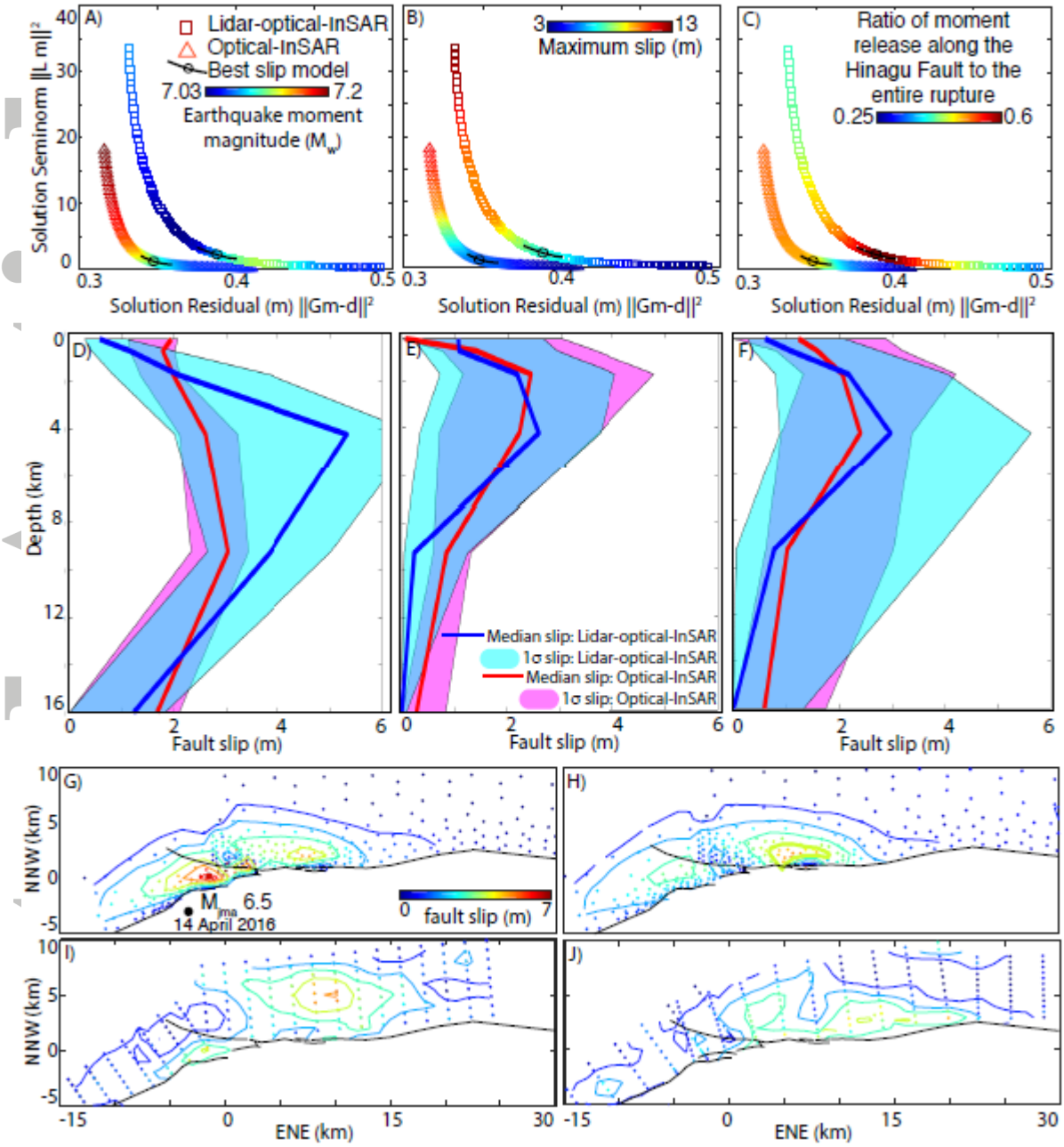

Figure 4: (A-C) L-curve showing solution seminorm vs residual for a variety of smoothing values (λ) for the lidar-optical-InSAR (squares) and the optical-InSAR (triangles) slip inversions. Colors show M_w (A), maximum slip (B), and ratio of moment release on the Hinagu fault to the entire earthquake (C). The black circle and curve symbol indicate the best slip model and uncertainty. (D-F) Median slip (blue and red line) vs depth for the Hinagu Fault (D), Futagawa fault (E), and entire earthquake (F). The cyan and pink clouds show the 1-σ slip range for the lidar-optical-InSAR and optical-InSAR slip inversions, respectively. G-J show map-view images of the slip distribution from (G) the lidar-optical-InSAR and (H) the optical-InSAR source inversion in this study as well as from (I) Asano & Iwata (2016) and (J) H. Kobayashi et al. (2017). Dots show modelled slip along subfaults, and the lines contour the fault slip. The black circle in (G) is the 14 April M_{JMA}6.5 foreshock epicenter location.